HHS Public Access

Author manuscript

Cell Rep. Author manuscript; available in PMC 2021 July 15.

Published in final edited form as:

Cell Rep. 2021 July 06; 36(1): 109310. doi:10.1016/j.celrep.2021.109310.

Compensatory hepatic adaptation accompanies permanent absence of intrahepatic biliary network due to YAP1 loss in liver progenitors

Laura M. Molina[1,2], **Junjie Zhu**[3], **Qin Li**[4], **Tirthadipa Pradhan-Sundd**[5,6], **Yekaterina Krutsenko**[2], **Khaled Sayed**[7,8], **Nathaniel Jenkins**[9], **Ravi Vats**[5,10], **Bharat Bhushan**[2,6], **Sungjin Ko**[2,6], **Shikai Hu**[2], **Minakshi Poddar**[2], **Sucha Singh**[2], **Junyan Tao**[2,6], **Prithu Sundd**[5], **Aatur Singhi**[11], **Simon Watkins**[9,12], **Xiaochao Ma**[3], **Panayiotis V. Benos**[7], **Andrew Feranchak**[4,6], **George Michalopoulos**[2,6], **Kari Nejak-Bowen**[2,6], **Alan Watson**[9,12], **Aaron Bell**[2,6], **Satdarshan P. Monga**[2,6,13,14,*]

[1]Medical Scientist Training Program, University of Pittsburgh School of Medicine, Pittsburgh, PA, USA

[2]Division of Experimental Pathology, Department of Pathology, University of Pittsburgh School of Medicine, Pittsburgh, PA, USA

[3]Department of Pharmaceutical Sciences and Center for Pharmacogenetics, University of Pittsburgh School of Pharmacy, Pittsburgh, PA, USA

[4]Division of Gastroenterology, Hepatology, and Nutrition, Department of Pediatrics, University of Pittsburgh School of Medicine and UPMC, Pittsburgh, PA, USA

[5]Division of Hematology/Oncology, Department of Medicine, University of Pittsburgh School of Medicine and UPMC, Pittsburgh, PA, USA

[6]Pittsburgh Liver Research Center, University of Pittsburgh and UPMC, Pittsburgh, PA, USA

[7]Department of Computational and Systems Biology, University of Pittsburgh, 3420 Forbes Ave, Pittsburgh, PA 15213, USA

[8]Biomedical Engineering and Systems, Faculty of Engineering, Cairo University, Giza, Egypt

[9]Center for Biologic Imaging, University of Pittsburgh, Pittsburgh, PA, USA

[*]Correspondence: smonga@pitt.edu.

AUTHOR CONTRIBUTIONS

Conceptualization: L.M.M. and S.P.M.; funding acquisition: L.M.M., S.P.M., S.W., A.S., and A.W.; investigation: L.M.M., J.Z., Q.L., T.P.-S., Y.K., K.S., N.J., R.V., B.B., S.K., S.H., M.P., S.S., J.T., P.V.B., A.W., and A.B.; methodology: L.M.M., A.W., S.W., M.P., and S.P.M.; resources: A.S., A.W., and S.W.; supervision: X.M., P.V.B., A.F., T.P.-S., P.S., K.N.-B., G.M., A.B., S.W., and S.P.M.; writing – original draft: L.M.M. and S.P.M.; visualization: L.M.M. and S.P.M.

SUPPLEMENTAL INFORMATION

Supplemental information can be found online at https://doi.org/10.1016/j.celrep.2021.109310.

DECLARATION OF INTERESTS

The authors declare no competing interests.

INCLUSION AND DIVERSITY

We worked to ensure sex balance in the selection of non-human subjects. One or more of the authors of this paper self-identifies as an underrepresented ethnic minority in science. One or more of the authors of this paper received support from a program designed to increase minority representation in science.

[10]Department of Bioengineering, School of Engineering, University of Pittsburgh, Pittsburgh, PA, USA

[11]Division of Anatomic Pathology, Department of Pathology, University of Pittsburgh School of Medicine and UPMC, Pittsburgh, PA, USA

[12]Department of Cell Biology, University of Pittsburgh School of Medicine, Pittsburgh, PA, USA

[13]Division of Gastroenterology, Hepatology, and Nutrition, Department of Medicine, University of Pittsburgh School of Medicine and UPMC, Pittsburgh, PA, USA

[14]Lead contact

SUMMARY

Yes-associated protein 1 (YAP1) regulates cell plasticity during liver injury, regeneration, and cancer, but its role in liver development is unknown. We detect YAP1 activity in biliary cells and in cells at the hepatobiliary bifur-cation in single-cell RNA sequencing analysis of developing livers. Deletion of *Yap1* in hepatoblasts does not impair Notch-driven SOX9+ ductal plate formation but does prevent the formation of the abutting second layer of SOX9+ ductal cells, blocking the formation of a patent intrahepatic biliary tree. Intriguingly, these mice survive for 8 months with severe cholestatic injury and without hepatocyte-to-biliary transdifferentiation. Ductular reaction in the perihilar region suggests extrahepatic biliary proliferation, likely seeking the missing intrahepatic biliary network. Long-term survival of these mice occurs through hepatocyte adaptation via reduced metabolic and synthetic function, including altered bile acid metabolism and transport. Overall, we show YAP1 as a key regulator of bile duct development while highlighting a profound adaptive capability of hepatocytes.

Graphical Abstract

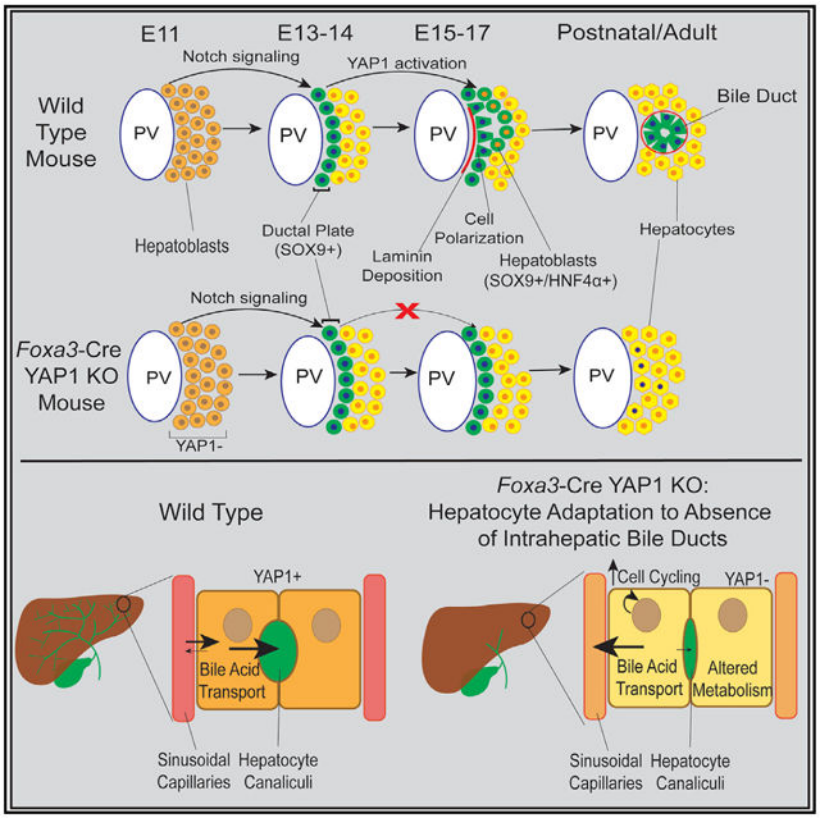

In brief

Molina et al. demonstrate that loss of *Yap1* in developing livers leads to absence of intrahepatic bile ducts, preventing bile secretion from liver to small intestines. Yap1 knockout mice are small and jaundiced and exhibit adaptation via altering bile acid transport and metabolism, but they eventually die around 8 months of age.

INTRODUCTION

The biliary tree is a delicate branching network of ducts formed of cholangiocytes, which transport bile from the liver to the intestines. Alagille syndrome is an autosomal dominant disorder arising from mutations in the *JAGGED1* or *NOTCH2* genes that cause multi-system malformations, including impaired formation of bile ducts in embryonic development (Mitchell et al., 2018). According to a recent prospective study, only about 24% of children with bile duct paucity reach adulthood without a liver transplant, indicating the serious need for alternative therapies (Kamath et al., 2020). The penetrance of these mutations varies widely, leading to variability in the extent of cholestasis and disease presentation, with some patients even showing spontaneous recovery. We lack an understanding of the disease modifiers and biomarkers that can help stratify or distinguish these patients during a critical treatment window (Emerick et al., 1999; Lykavieris et al., 2001; Mitchell et al., 2018).

Yes-associated protein 1 (YAP1) is a transcriptional co-activator and mechanosensor thatmodulates cell differentiation, proliferation, and survivalamong liver cells, depending on

the context (Patel et al., 2017). Studies have shown that YAP1 is important for bile duct development and homeostasis, although its exact role remains poorly understood (Lee et al., 2016; Pepe-Mooney et al., 2019; Yimlamai et al., 2014; Zhang et al., 2010). Albumin (Alb)-Cre-mediated deletion of YAP1 in late stages of murine liver development led to bile duct paucity postnatally, causing unresolved cholestatic injury (Zhang et al., 2010). Similarly, activation of YAP1 through Alb-Cre-mediated deletion of upstream negative regulators LATS1/2 resulted in abnormal overgrowth of ductular cells and, *in vitro*, facilitated hepatic progenitor differentiation into biliary epithelial cells (BECs) (Lee et al., 2016). Other studies have shown YAP1 is a major driver of hepatoblastoma, a pediatric liver tumor, and can dedifferentiate mature hepatocytes into hepatoblasts (HBs) in a murine model (Alder et al., 2014; Molina et al., 2019; Tao et al., 2014). Thus, the role of YAP1 in hepatobiliary differentiation remains ambiguous.

Hepatobiliary plasticity is being increasingly appreciated. Chronic injury to the bile ducts in rodents induced transdifferentiation of hepatocytes into cholangiocytes to promote repair (Michalopoulos et al., 2005; Okabe et al., 2016; Schaub et al., 2018; Sekiya and Suzuki, 2014; Yanger et al., 2013). This was convincingly observed in an animal model of Alagille syndrome with liver-specific developmental ablation of Notch signaling (Schaub et al., 2018). Despite the total failure of intrahepatic bile duct (IHBD) formation, many of these mice recovered and survived long term because of hepatocyte-derived *de novo* generation of bile ducts (Schaub et al., 2018). Phenotypic recovery over time has also been observed in some murine models of Alagille syndrome (Andersson et al., 2018; Thakurdas et al., 2016). Although YAP1 can promote the expression of biliary markers in mature hepatocytes (Yimlamai et al., 2014) and is a potential regulator for Notch signaling (Kim et al., 2017; Tschaharganeh et al., 2013) (even in a mouse model devoid of the Notch co-factor RBPJ; Tharehalli et al., 2018), it is not known whether YAP1 activation is essential or dispensable for cells to adopt a biliary phenotype or to assemble into functional ductular structures.

In this study, we address the role of YAP1 during the earliest stages of embryonic liver development, demonstrating its indispensable role in bile duct morphogenesis. The conditional loss of YAP1 in HBs led to failure of intrahepatic biliary tree generation, reminiscent of Alagille syndrome, as demonstrated using various functional studies and innovative three-dimensional (3D) imaging. Furthermore, we characterize the compensatory metabolic and synthetic adaptations that allow mice with severe cholestatic injury to survive long term.

RESULTS

Loss of YAP1 in HBs during early embryonic development leads to absence of intrahepatic bile duct formation and severe chronic cholestatic injury

To assess the status of YAP1 activity in liver development, we analyzed single-cell sequencing data published by Yang et al. (2017) for the expression of YAP1 targets. The study assessed the differentiation of HBs into hepatocytes and cholangiocytes from embryonic day (E) 10.5 to E17.5. We identified three clusters closely matching the cell identities assigned by Yang et al. (2017), clearly distinguishing the trajectory of differentiation over pseudotime of HBs (cluster a) into hepatocytes (cluster c) and

cholangiocytes (cluster b) (Figures S1A and S1B). When comparing gene expression in these clusters, we observed that the expression of canonical YAP1 targets *Ccn1* and *Ccn2* was notably increased in the cholangiocyte cluster over the pseudotime axis while remaining low in the HB and hepatocyte clusters (Figures S1C and S1D). We also found that several cells from early time points E11.5–E14.5 were classified differently by our methods in comparison to those previously published and express both *Sox9* and *HNF4α*, suggesting they may be cells of intermediate differentiation (Figures S1A and S1B). YAP1 target gene expression in these cells (cluster d) is somewhat higher than in most HBs but lower than most cholangiocytes (Figure S1C), suggesting that YAP1 activity is increasing in these intermediate cells as they transition into cholangiocytes.

Previous studies have used *Alb*-Cre to delete YAP1 in the liver to elucidate its functions. However, in this model, recombination occurs around E15–E16 and is not completed until 4–6 weeks postnatally (Postic and Magnuson, 2000). Because the process of cholangiocyte differentiation from HBs begins earlier, around E11.5 (Su et al., 2017; Yang et al., 2017), we targeted YAP1 in HBs at the earliest stages of development. Because *Foxa3* is activated in the foregut endoderm progenitors, including HBs, starting at E8.5 and achieving complete recombination around E12–E13 (Lee et al., 2005; Tan et al., 2008), we bred *Foxa3*-Cre transgenic to YAP1-floxed mice and generated HB-YAP1 knockout (YAP1 KO) mice. Immunofluorescence (IF) imaging for YAP1 at E14.5 shows complete loss of YAP1 from HNF4α-labeled HBs (Figure S1E).

Although we expected to observe a more widespread effect, YAP1 KO mice formed all foregut organs and were viable postnatally, with some mice surviving up to 8 months, at which time they were sacrificed for study. We calculated the observed genotype frequencies for harvested embryos and for adult mice (postnatal day [P] 21 or later), as shown in Table 1. We found that embryos up to E18 are harvested at the expected genotype frequency of 50% wild type (WT), 25% heterozygous (HET), and 25% YAP1 KO. However, adult mice show a significant alteration in genotype frequencies, with 59% WT, 26% HET, and 16% YAP1 KO (chi-square test, $p = 0.00099$). Thus, we observe a loss of YAP1 KO mice in the early postnatal period of about 36%.

Grossly, mice who survived displayed stunted growth and were visibly jaundiced (Figure 1A), with significantly lower body weight than WT littermates, although their liver weights were comparable to those of WT mice, resulting in an increased liver weight-to-body weight ratio (Figures 1B–1D). At P21, YAP1 KO mice showed elevated alkaline phosphatase, total bilirubin, and direct bilirubin levels and significantly elevated aspartate aminotransferase and alanine aminotransferase (AST and ALT), indicating severe hepatocellular and cholestatic injury (Figures 1E–1H). H&E staining displayed numerous biliary infarcts (Figure S1F). Immunohistochemistry (IHC) for YAP1 in adult knockout (KO) mice showed persistent complete YAP1 loss in all liver epithelial cells but retained YAP1 staining in endothelial cells and other non-parenchymal cells, compared with WT, which showed low levels of cytoplasmic YAP1 in most hepatocytes and strong nuclear YAP1 in mature bile ducts (Figures 1I and 1L). CK19 staining shows that although WT livers have well-formed bile ducts surrounding the portal veins throughout the liver, YAP1 KO mice demonstrated an absence of defined ductal structures except for a few ducts limited to the perihilar region and

even fewer large ducts extending occasionally into the median hepatic lobe (Figures 1J, 1K, and 1M). SOX9 staining in adult KO livers revealed unstructured clusters of SOX9+ cells around the portal vein, in contrast to well-formed SOX9+ patent bile ducts in WT (Figure S1G). Similarly, epithelial cellular adhesion molecule (EpCAM) staining revealed absence of ductal structures in KO livers with significant hepatocyte upregulation of EpCAM, in contrast to well-formed EpCAM+ bile ducts in WT (Figure S1H).

Surprisingly, YAP1 KO mice survived for more than 8 months, when they were euthanized due to progressive morbidity. Even though markers of cholestatic injury remained severely elevated throughout, AST and ALT returned to almost normal levels by 3 months of age, suggesting that these injured livers deployed some adaptive mechanisms to survive despite severe cholestasis (Figures 1E–1H).

Overall, YAP1 KO mice exhibited significant failure to thrive and cholestatic injury, associated with persistent lack of intrahepatic bile ducts in the postnatal liver, resembling an Alagille syndrome-like phenotype.

YAP1 KO mice show no hepatocyte-driven biliary regeneration but exhibit limited DR around hilum, arising from extrahepatic bile ducts

We next investigated repair mechanisms that may be allowing YAP1 KO to survive long term. Previous studies have convincingly demonstrated the capacity of normal hepatocytes to transdifferentiate to regenerate *de novo* bile ducts in the setting of similar developmental biliary defects *in vivo* (Schaub et al., 2018). Hence, we first evaluated whether similar evidence of biliary regeneration occurred over time in YAP1 KO. Intriguingly, we found no YAP1-negative bile ducts even up to 8 months. Most of the liver remained devoid of intrahepatic ducts. To unequivocally demonstrate this, we visualized the 3D structure of the bile ducts in WT and YAP1 KO mice at P21 and 8 months using a tissue-clearing protocol we developed specifically for liver tissue, combined with ribbon scanning confocal microscopy, to achieve 3D IF staining of whole liver tissue (Figures 2A–2D; Video S1). CK19 staining clearly delineated the hierarchical branching biliary network in P21 and 8-month-old WT mice, which was absent from YAP1 KO mice at both times except for a few ducts in the perihilar region connected to the extrahepatic biliary tree and gallbladder. We corroborated this finding using India ink injections into the common bile duct followed by tissue clearing to visualize the ink-traced biliary network and observed no ducts in adult KO mice (Figure S2A). Thus, we unambiguously demonstrate the gross absence of biliary regeneration in YAP1 KO mice.

We noticed a ductular reaction (DR), albeit only in the perihilar region and particularly in the median lobe of the mouse liver. This DR consisted of YAP1-positive ducts and was associated with significant inflammation and fibrosis surrounding the largest portal veins (Figures 2E and 2F; Figures S1H and S1I). To assess the source of DR, we wondered whether the YAP1-positive ducts could have arisen from YAP1-positive hepatocytes that may have escaped Cre recombination and could have transdifferentiated into BECs. However, no YAP1-positive hepatocytes were observed by IHC (Figure 1L). IF showed that although DR in the hilar region was YAP1 positive, the surrounding hepatocytes were YAP1 negative (Figure 2G). Using a ROSA-stop$^{fl/fl}$-EYFP reporter, we verified that >99% of

hepatocytes (HNF4α+) in YAP1 KO mice were EYFP positive, demonstrating successful Cre recombination (Figures 2H and 2I). Thus, we rule out hepatocytes as a source of the DR and show that YAP1-negative hepatocytes are not capable of transdifferentiating into biliary cells, validating the role of YAP1 in hepatocyte transdifferentiation (Fitamant et al., 2015; Yimlamai et al., 2014).

To substantiate the functional absence of an intrahepatic biliary tree while assessing whether the regional DR contributed functionally, we measured the bile flow rate by cannulating the common bile duct, which is present in both WTs and YAP1 KOs. Bile flow at the expected rate in an unstimulated setting was seen in WT mice, but there was no detectable bile flow in YAP1 KO mice (Figure 3A). Altogether, we show persistent lack of an intrahepatic biliary tree and a DR from extrahepatic ducts restricted mostly to the perihilar region, which was insufficient to restore function through intrahepatic biliary repair in YAP1 KO mice.

Gene expression changes in YAP1 KO livers indicate global metabolic and synthetic changes, including in bile acid homeostasis as an adaptation to the absence of bile ducts

Because biliary regeneration was not the basis of prolonged survival in the YAP1 KO, we posited that several adaptations to chronic cholestatic injury may be in play. We performed RNA sequencing (RNA-seq) analysis on adult YAP1 KO mice and WT mice, using both males and females in each group for comparison. Principal-component analysis showed WT and KO mice to be distinguished by the first principal component (Figure S2B). Comparison of YAP1 KO and WT livers identified 2,606 differentially expressed genes (false discovery rate [FDR] < 0.05, abs(FC) > 2). Pathway analysis using various common software algorithms—Ingenuity Pathway Analysis (IPA; QIAGEN), gene set enrichment analysis (GSEA) (Subramanian et al., 2005), and Enrichr (Kuleshov et al., 2016)—was performed, and similar observations were evident. Both pathway analysis and transcription factor enrichment analysis highlighted robust activation of innate and adaptive immune responses in YAP1 KO mice, along with stellate cell activation and fibrosis (Figures S2C, S2D, S2H, and S2I). This is consistent with histological evidence of increased pericellular fibrosis and the presence of inflammatory cell clusters in adult KO (Figures S1H and S1I).

In addition, we observed an increase in pathways related to proliferation, cell cycling, and cancer, alongside downregulation of mature metabolic and synthetic genes normally expressed in hepatocytes (Figures S2E, S2H, and S2I). This is consistent with our observation of increased hepatocyte proliferation in adult KO mice relative to WT through IHC for Ki67 (Figures S2F and S2G). We also observed significant downregulation of metabolic and synthetic pathways related to fatty acid oxidation, oxidative phosphorylation, xenobiotic metabolism, and bile acid and sterol metabolism, all of which are hallmarks of mature liver function (Figure 3B). Decreases in fatty acid oxidation have been previously described in multiple cholestatic diseases in mice and patients and shown to be related to decreased PPARα activity, which was supported in YAP1 KO by IPA and Enrichr analysis (Figures S2H and S2I) (Katzenellenbogen et al., 2007; Pablo Arab et al., 2017; Zhao et al., 2017). Decreased gene expression related to bile acid and sterol metabolism suggested inactivation of FXR, RXR, and LXR transcription factors (Figure S2I). Likewise, expression of most enzymes involved in the classic and alternative bile acid synthesis pathways were

downregulated in YAP1 KO livers (Figure 3C). Interestingly, expression of most apical and basolateral transporters regulating bile acid transport in hepatocytes was altered to favor increased secretion back into the sinusoids rather than the hepatocyte apical canaliculi (Figures 3D–3F).

To determine whether these changes result directly from the loss of YAP1 in hepatocytes, we used a previously published dataset to compare gene expression patterns in WT mice to $YAP1^{fl/fl}$ mice injected with hepatocyte-specific adeno-associated virus serotype 8 expressing Cre recombinase, thus creating a hepatocyte-specific adult knockout of YAP1 (YAP1 HepKO) (Bhushan et al., 2021). Gene expression was determined by Affymetrix microarray analysis and showed no significant differentially expressed genes in YAP1 HepKO relative to littermate control WT mice. Thus, the observed gene expression changes in our developmental YAP1 KO model do not result from YAP1-specific deregulation but rather are part of a global program of genetic adaptation to chronic cholestatic injury.

To assess the functional consequences of these gene expression changes, we performed quantitative and qualitative analysis of bile acids in YAP1 KO mice compared with WT in both liver tissue and serum. The total quantity of bile acids was dramatically increased in the liver (~6×) and in the serum (~40×) in YAP1 KO mice (Figure 3G), suggesting the general decrease in bile acid synthetic enzyme expression to be compensatory. Next, in the KOs, the diversity of species normally found in WT mice was overwhelmingly shifted in favor of primary conjugated bile acids, particularly taurocholic acid (TCA) and taurobetamurocholic acid (TβMCA), which individually were increased by almost 1,000-fold in the serum, whereas less soluble primary unconjugated bile acids were significantly decreased in liver tissue (Figure 3I; Figures S3A–S3L). Secondary bile acids derived from bacterial digestion of primary bile acids in the gut were also significantly decreased in liver and serum of KO mice (Figures S3A–S3L). Using previously published data on bile acid hydrophobicity (Heuman, 1989), we show that the bile acid pool in both liver and serum of YAP1 KO mice exhibited significantly lower hydrophobicity indices compared with WT, indicating a shift toward more soluble bile acid species to reduce their toxicity and facilitate their secretion into the blood (Figure 3H).

We next used intravital microscopy to visualize the flow of bile from hepatocytes into the canaliculi in WT and KO (Figure 3J; Video S2). In WT mice, carboxy-fluorescein-di-acetate (CFDA) injected into the bloodstream was taken up by hepatocytes, metabolized into carboxyfluorescein (CF) to fluoresce green, and exported into the hepatocyte canaliculi, providing a clear view of the tightly sealed canalicular network segregated from the capillary blood flow (dyed red using Texas red dextran). In contrast, in YAP1 KO livers, none of the CF entered the canaliculi, which could not be visualized. There was notable mixing of blood and bile, as shown by yellow in the capillaries, suggesting hepatocyte-metabolized CF transport back into the blood (Figure 3J; Video S2). To verify that this finding did not result from the absence of hepatocyte canaliculi, we used staining for CEACAM1 to visualize the hepatocyte canaliculi in WT and KO mice. Figure S3M shows that YAP1 KO hepatocytes are appropriately polarized and form canaliculi like WT hepatocytes, although there is some canalicular dilatation, which is a classic feature of cholestatic disease (Valencia-Mayoral et al., 1984).

Thus, these transcriptional and functional adaptations reflect a concerted effort to remove bile acids from liver by exporting them into the serum while reducing their toxicity through conjugation in an attempt to limit hepatocellular injury.

YAP1 loss does not impair Notch-driven ductal plate formation but interferes with ductal plate cell polarization and maturation of the second layer of ductal cells, impairing bile duct morphogenesis

YAP1 has previously been suggested to play a role in the formation of bile ducts in embryonic development, but an underlying mechanism has remained elusive. We first show in WT mice that YAP1 is indeed present in the nuclei of ductal plate cells and maturing bile ducts at E16.5, whereas YAP1 is absent from hepatoblasts and developing ducts in YAP1 KO mice (Figure S4A).

To investigate, we closely examined previously described stages of intrahepatic bile duct formation in YAP1 KO livers, using SOX9 as a marker of cells that are adopting cholangiocyte specification. SOX9-positive cells representing the initial formation of the ductal plate were similarly evident around the portal veins at E14.5 and E16.5 in the WT and YAP1 KO (Figures 4A and 4B). HES1, a downstream target of Notch signaling, was similarly expressed in the ductal plate cells of the WT and KO embryonic livers (Figure S4B), suggesting initial activation of Notch signaling in putative BECs is not affected by YAP1 loss. Furthermore, expression of JAGGED1 in ductal plate cells was not changed in YAP1 KO relative to WT (Figure S4C).

Between E16.5 and E17.5, SOX9 staining in WT livers revealed a hierarchical formation of luminal structures, lined on one side by the previously described pre-existing SOX9-positive ductal plate cells (Figure 4C, insets 1 and 2) and on the other side by another layer of SOX9-positive cells thought to be derived from HBs, which lose HNF4α and gain SOX9 to adopt a BEC identity (Figure 4C, inset 3) (Ober and Lemaigre, 2018). At comparable time points, YAP1 KOs showed disparate ductal morphology. At E17.5, we observed formation of only a few pseudoluminal structures in YAP1 KO closest to the largest portal vessels (Figure 4C, insets 5 and 6), which were lined by SOX9-positive cells, albeit only on the portal side. Moreover, we failed to observe real ducts lined completely by the second layer of SOX9-positive cells (Figure 4C). Postnatally, YAP1 KO mice continued to retain a single layer of SOX9+ cells around the portal veins showing no signs of luminal structures (Figure 4D). The parenchymal or the second layer of would-be biliary cells in nascent ducts consistently retained HNF4α in KO, whereas in WT, these cells lose HNF4α and gain SOX9 expression as they mature into BECs (Figure 4C). This resulted in an overall increase in the number of HNF4α-positive cells in E17.5 KO livers compared with matched WT (Figures S4D and S4E). HNF4α also seemed to be expressed in the nuclei of some YAP1 KO ductal plate cells, as seen in Figure S4A.

Because we observed the appearance of some pseudoluminal biliary structures, we next queried whether primitive biliary cells in YAP1 KO mice successfully establish polarity. We used IF for acetylated α-tubulin to visualize primary cilia, which are critical for sensing bile flow and regulating numerous growth factor signaling pathways (Mansini et al., 2018). WT cholangiocytes in maturing bile ducts first displayed diffuse staining for acetylated tubulin

throughout their cytoplasm, which gradually developed into precise punctate staining at the apical surface in both layers of ductal cells (Figure 4B, yellow arrows). In contrast, in YAP1 KO mice the ductal plate cells express acetylated tubulin in a diffuse pattern, with almost no puncta visible (Figure 4B). This suggests impaired establishment of polarity in maturing portal cholangiocytes in KO mice.

Crosstalk between the ductal plate and the adjacent portal mesenchyme is also critical for bile duct morphogenesis (Ober and Lemaigre, 2018). Specifically, portal fibroblasts deposit laminins containing laminin-α1 on the portal side of the ductal plate to provide a foundation, and later, ductal cells deposit laminin-α5 in their surrounding basal lamina (Ober and Lemaigre, 2018; Tanimizu et al., 2012). Using a pan-laminin antibody, we show that WT ductal cells exhibit deposition of laminin first on the basolateral side closest to the portal vein and later surrounding the maturing duct (Figure 4C, yellow arrows). KO BECs showed only weak to no laminin deposition even on the portal side and failed to robustly deposit laminin around ductal cells (Figure 4C, white boxes), whether HNF4α positive or negative, and the only laminin observed in KO mice was lining the blood vessels.

Altogether, these data suggest that YAP1 loss does not alter Notch signaling in the ductal plate but rather prevents maturation of ductal plate cells and advancement of ductal morphogenesis by impairing cell polarization and laminin deposition. YAP1 loss also results in persistent HNF4α expression in hepatoblasts adjacent to the ductal plate and even among some cells of the ductal plate.

DISCUSSION

By directly knocking out YAP1 from HBs, we addressed the role of YAP1 in the earliest stages of liver development. We show that YAP1 is not necessary for Notch-driven initiation of biliary differentiation in the ductal plate and YAP1 loss does not impair Notch signaling in the ductal plate. However, YAP1 loss interferes with establishment of polarity in the ductal plate, laminin deposition in the basolateral side of the ductal plate, and loss of HNF4α expression in HBs adjacent to this layer. We observed a clear layer of Sox9-positive, HNF4α-negative BECs closest to the portal mesenchyme at E14.5 and before, suggesting the existence of these biliary-committed cells already at this stage. However, the second layer of BECs appears to be strictly YAP1 dependent and critical in switching the fate of adjacent HBs to BECs and in their incorporation into the growing ducts. Thus, YAP1 is an essential mediator of BEC maturation in the ductal plate and for the progression of BEC morphogenesis (Ober and Lemaigre, 2018).

Several hypotheses explain the molecular basis of this defect, requiring future studies. First, YAP1 may be involved in the establishment and maintenance of cell polarization in ductal plate cells, as well as adjacent HBs. A recent study showed that Anks6, a protein localized to the primary cilium of developing ductal plate cells, regulates YAP1 transcriptional activity, and loss of Anks6 results in defects of bile duct morphogenesis (Airik et al., 2020). Although this suggests that YAP1 activity in the ductal plate depends on appropriate polarization, our data suggest that YAP1 loss impairs primary cilium formation and

polarization, pointing to a positive feedback loop that may be required for maintenance of bile duct cell polarity.

Second, YAP1 may be involved in cell-cell communication from the portal mesenchyme to ductal plate cells, as well as from ductal plate cells to adjacent HBs, which may also depend on proper polarization of ductal plate cells. This may or may not be occurring downstream of Notch signaling. A previous study suggested that overgrowth of bile ducts because of *Alb*-Cre Nf2 deletion and subsequent YAP1 activation was ablated by *Notch2* deletion, suggesting Notch activity is downstream of YAP1 in bile duct development (Wu et al., 2017). However, *Notch2* deletion in this model did not prevent bile duct formation, and these mice exhibited limited injury. Our data, in which YAP1 deletion occurs early during biliary differentiation, suggest Notch signaling is upstream of YAP1 activation in the ductal plate but downstream of YAP1 signaling in the second layer of HBs. YAP1 has been shown to regulate *Notch2* and *Jagged1* gene expression (Lee et al., 2016; Tschaharganeh et al., 2013).

Third, transforming growth factor β (TGF-β) signaling originating from the portal mesenchyme is critical for the formation of the second layer during bile duct morphogenesis (Antoniou et al., 2009; Clotman et al., 2005; Lee et al., 2016) and a known driver of hepatocyte-derived biliary regeneration in a model of Alagille syndrome in which Notch signaling was impaired (Schaub et al., 2018). YAP1 may be a downstream effector of TGF-β signaling in HBs to regulate their fate switch to form a second layer of biliary cells, downregulating HNF4α in second-layer HBs (Lee et al., 2016). It has been shown that YAP1 can regulate both HNF4α expression and its genome binding distribution, so YAP1 may be critical for turning off a hepatoblast/hepatocyte genetic program in favor of a Notch-driven biliary program (Alder et al., 2014; Lee et al., 2016). Finally, YAP1 can influence secretion of extracellular matrix components such as laminin-α5 (Gérard et al., 2017; Ober and Lemaigre, 2018), which was deficient around developing ducts in YAP1 KO mice. Interrupting integrinlaminin signaling during bile duct morphogenesis results in defects similar to YAP1 KO (Tanimizu et al., 2012). Some or all of these molecular events may be contributing to the observed phenotypic defect.

We did not detect biliary regeneration through hepatocyte transdifferentiation in our Alagille syndrome-like model, in contrast to other studies (Andersson et al., 2018; Schaub et al., 2018; Tharehalli et al., 2018; Walter et al., 2014). Our results demonstrate an absolute YAP1 requirement in hepatocytes to undergo transdifferentiation into cholangiocytes. Although other studies have shown YAP1 activation drives expression of biliary markers in hepatocytes and promotes formation of hepatocyte-derived cholangiocarcinoma (Li et al., 2015; Wang et al., 2018; Yimlamai et al., 2014), we provide evidence that without YAP1, the liver cell identity shift cannot occur.

Our model also provides an opportunity to study the relationship between IHBDs and extrahepatic bile ducts (EHBDs), which remains poorly understood (Lemaigre, 2020). *Foxa3*-Cre did not affect *Yap1* expression in EHBDs, including the gallbladder, all of which formed normally. Using tissue clearing and confocal imaging, we were able to visualize the gallbladder, cystic duct, and perihilar ducts entering the median lobe in both WT and KO

mice. Our two-dimensional (2D) and 3D imaging showed that the EHBDs extend farther into the median lobe than other liver lobes. We posit that the ductular reaction observed in adult KO mice arises from EHBDs responding to severe cholestatic injury. This response, which is accompanied by fibrosis and inflammation (Alvaro et al., 2007), is primarily associated with large portal vessels in KO mice and may be an attempt of EHBDs to expand to try and locate and connect with IHBDs, which are lacking in KO. Our model demonstrates that the EHBDs are unable to regenerate IHBDs, similar to previous studies (Schaub et al., 2018), although enabling such a process may provide novel therapies in the future.

Despite the severity of liver disease in YAP1 KO mice, they survived long term by adapting and reprogramming metabolic, synthetic, and detoxification functions while enhancing proliferation and survival signaling. Such adaptations have been reported in other models of liver disease, such as Mdr2 KO and combined hepatic Met-EGFR loss (Katzenellenbogen et al., 2007; Paranjpe et al., 2016). YAP1 KO mice invert their bile acid transport to overcome the lack of plumbing for bile excretion. Although this led to elevated levels of bile acids and bilirubin in the blood, these toxic components were eliminated from hepatic parenchyma, thereby reducing hepatocellular injury. Persistently elevated serum total and conjugated bilirubin levels in young children with Alagille syndrome are associated with more severe liver disease and decreased the likelihood of spontaneous improvement over time, similar to that seen in our model (Kamath et al., 2010). The same adaptive changes in bilirubin and bile acid transport observed in YAP1 KO mice may be occurring in patients with severe disease and may indicate maximal hepatocyte adaptation in the context of failed biliary regeneration. Thus, YAP1 activation may be an important disease modifier in patients with Alagille syndrome and other biliary disorders, requiring further studies. Overall, the surprising capacity of the liver to survive and adapt may be harnessed therapeutically to better understand how to support patients with chronic liver injury.

STAR★METHODS

RESOURCE AVAILABILITY

Lead contact—Further information and requests for resources and reagents should be directed to and will be fulfilled by the Lead Contact, Satdarshan Monga (smonga@pitt.edu).

Materials availability—Any and all tissue samples and mice described in this paper can be made available under a fully executed Materials Transfer Agreement. Please contact the corresponding author for details.

Data and code availability—RNA-sequencing data generated in this study are available at GEO: GSE157777.

EXPERIMENTAL MODEL AND SUBJECT DETAILS

Animal models—C57BL/6 YAP1$^{fl/fl}$ mice (Jackson Labs Stock No. 027929) (Zhang et al., 2010) were bred into C57BL/6 ROSA-stop$^{fl/fl}$-EYFP mice. These mice were then bred into C57BL/6 *Foxa3*-Cre mice described previously (Tan et al., 2008) to create *Foxa3*-Cre

YAP1$^{fl/fl}$ ROSA-stop$^{fl/fl}$-EYFP mice (YAP1 KO). Wild-type littermate controls were compared to YAP1 KO mice for all subsequent analyses. All animal studies were performed in accordance with the guidelines of the Institutional Animal Use and Care Committee at the University of Pittsburgh School of Medicine and the National Institutes of Health. All animals were group housed in ventilated cages under 12h light/dark cycles with access to enrichment, water and standard chow diet *ad libitum* unless otherwise specified. Both male and female mice were used throughout the study and littermates were used as WT controls. Mice were analyzed at the following time points: E14.5, E16.5, E17.5, P9, P21, 3–4 months, and 6–8 months of age. Analysis of serum liver function tests was performed by the clinical laboratories at University of Pittsburgh Medical Center (UPMC).

METHOD DETAILS

scRNA-seq raw data retrieval and processing—The raw sequencing data files were downloaded from public dataset GEO:GSE90047 using the SRA toolkit with the “fastq-dump–split-files” command (http://ncbi.github.io/sra-tools/). The single-end reads were then quantified and aligned using kallisto algorithm with “kallisto quant -i index_file -o output_file -t64–pseudobam–single -l 51 -s 1 fastq_file.” (Bray et al., 2016) We also used the “samtools sort” command (Li et al., 2009) to sort the aligned bam files before we ran Velocyto (La Manno et al., 2018) to create loom files with the command “velocyto run -e sample_id–onefilepercell–without-umi sorted_bam_file Mus_musculus.GRCm38.100.gtf.” The loom files, which contain the data matrices, were then merged to a single file using the “loompy.combine” function on Python. Finally, the Seurat-Wrappers function “ReadVelocity()” was used to read the combined loom file and convert it to a single-cell gene expression count matrix (Stuart et al., 2019).

scRNA-seq data analysis—We used Seurat and Monocle packages to perform the single-cell and the pseudotime analyses (Stuart et al., 2019; Trapnell et al., 2014) The count matrix was first converted into a Seurat object and then the data was normalized and scaled using Seurat functions NormalizeData() and ScaleData(), respectively. The top 5000 highly variable genes were then selected for the downstream analysis using the Seurat:FindVariableFeatures() function with selection.method = “disp” which selects the genes with the highest dispersion values. The top 5000 highly variable genes were used to perform principal component analysis which was conducted using the Seurat:RunPCA() function. The first 10 principal components were used for Louvain clustering and tSNE visualization (Seurat functions FindClusters() and RunTSNE(), respectively). The expression values of the genes were visualized using Seurat function VlnPlot(). The Pseudotime analysis was performed using the Monocle package following the three standard workflow steps which include choosing genes that define cells’ progress (i.e., feature selection), reducing the data dimensionality using the reverse graph embedding algorithm (Mao et al., 2017), and ordering the cells in pseudotime. The Monocle function plot_genes_in_pseudotime() was used to create Figure S1D which shows the expression levels of the genes of interest as a function of the differentiation pseudotime.

Immunostaining—Adult livers were harvested and fixed in 10% formalin for 48 hours, then transferred into 70% ethanol followed by paraffin embedding at the UPMC clinical

laboratories. Embryonic and fetal livers were harvested and fixed in 4% paraformaldehyde (PFA) for 24 hours at 4C, followed by paraffin embedding. For immunostaining, 4 μm paraffin sections were cut, deparaffinized and rehydrated. Sections underwent antigen retrieval by the following methods: 1) pressure cooker, 20 minutes, in sodium citrate buffer pH 6 (YAP1, SOX9, HNF4α, EYFP, CK8, pan-laminin, HES1, CK19 for IF); 2) pressure cooker, 20 minutes, in Agilent DAKO (S1699) target retrieval solution (EpCAM, CK19 for IHC); 3) microwave, 60% power, 12 minutes, in sodium citrate buffer pH 6 (CK8, acetylated tubulin, JAGGED1, HNF4α, CEACAM1); 4) steamer, 20 minutes, in sodium citrate buffer pH 6 (CD45).

At this point, for immunohistochemistry, slides were treated with 3% H_2O_2 for 10 minutes to deactivate endogenous peroxidases, washed three times with PBS, then blocked for 10 minutes with SuperBlock reagent (ScyTek Laboratories, AAA500). Slides were incubated in primary antibody diluted in PBS with 0.1% bovine serum albumin (BSA) and 0.01% sodium azide (IHC buffer), for either 1 hour at room temperature (CD45 1:100, CEACAM1 1:100) or overnight at 4C (YAP1 1:50, SOX9 1:2000, CK19 1:50, EpCAM 1:50). Slides were then washed three times with PBS and incubated in the appropriate biotinylated secondary antibody at 1:500 dilution for 30 minutes at room temperature. Samples were washed with PBS three times and sensitized with the Vectastain ABC kit (Vector Laboratories, PK-6101) for 30 minutes. Following three washes with PBS color was developed with DAB Peroxidase Substrate Kit (Vector Laboratories, SK-4100), followed by quenching in distilled water for five minutes. Slides were counterstained with hematoxylin (Thermo Scientific, 7211), dehydrated to xylene and coverslips applied with Cytoseal XYL (Thermo Scientific, 8312-4). Images were taken on a Zeiss Axioskop 40 inverted brightfield microscope. Whole slides were scanned at 40x magnification using an Aperio AT2 slide scanner (Leica Biosystems).

For immunofluorescence staining, following deparaffinization, rehydration, and antigen retrieval as listed above, sections were permeabilized for 5 minutes with PBS/0.3% Triton X-100 and blocked for 45 minutes in PBS/0.3% Triton X-100/10% BSA. Slides were incubated at 4C overnight in primary antibody cocktails diluted in PBS/0.3% Triton X-100/10% BSA at the following concentrations: CK8, 1:8; all others, 1:100. Slides were washed three times in PBS/0.1% Triton X-100 and incubated at room temperature in secondary antibody cocktails (Invitrogen) also diluted in PBS/0.3% Triton X-100/10% BSA, for 1 hour (dilution 1:500) or 2 hours (dilution 1:800). Slides were again washed three times in PBS/0.1% Triton X-100, then washed three times in PBS, and mounted and coverslipped using VECTASHIELD Antifade Mounting Medium with DAPI (Vector Labs). Slides were imaged on a Nikon Eclipse Ti epifluorescence microscope or LSM 700 Carl Zeiss confocal microscope. Cell and nuclei quantification was performed using Fiji/ImageJ (Schindelin et al., 2012).

For H&E staining, samples were deparaffinized and stained with hematoxylin (Thermo Scientific, 7211) and eosin (Thermo Scientific, 71204), followed by dehydration to xylene and application of a coverslip. For Sirius Red staining, samples were deparaffinized and incubated for one hour in Picro-Sirius Red Stain (American MasterTech, STPSRPT),

washed twice in 0.5% acetic acid water, dehydrated to xylene, and coverslipped. Images were taken on a Zeiss Axioskop 40 inverted brightfield microscope.

Liver tissue clearing and whole liver immunostaining—Livers were washed in PBS and tissue fixation was achieved by incubating either whole livers or individual liver lobes in 4% paraformaldehyde (PFA) for 24 hours at 4C. Livers were subsequently washed in PBS and stored long-term in PBS/0.1% sodium azide (PBSA) at 4C.

Tissues were incubated in an inactive hydrogel solution overnight at 4C, consisting of 4% acrylamide (Bio-Rad 161-0140), 0.05% bis-acrylamide (Bio-Rad 161-0142), and 0.25% (wt/vol) VA-044 dissolved in PBS. The hydrogel solution was then polymerized by placing the tissues in a water bath at 37C for 3 hours (Chung et al., 2013; Muntifering et al., 2018). Excess hydrogel was removed, tissues were washed in PBS, and then tissues were placed in the X-CLARITY clearing apparatus (LogosBio C30001). Tissues were cleared using X-CLARITY-ETC Tissue Clearing Solution (LogosBio C13001) supplemented with 10–20mL of N,N,N′,N′-Tetrakis(2-Hydroxypropyl)ethylenediamine (Quadrol) for every 1.5L of clearing solution. The clearing apparatus was run at 37C with constant fluid circulation (100rpm peristaltic pump setting) and a setting of maximum current and voltage set at 1.5 Amps and 70 V respectively. Timing of tissue clearing varied based on the size of the liver lobes and ranged from 24 hours (smallest lobes, 1000×1000×3mm) to 72 hours (large lobes, 2000×2000×5mm). Next, tissues were washed with PBSA and incubated in 3% H_2O_2 for 24 hours. At this stage, after washing with PBSA, tissue could be stored long-term in PBSA at room temperature or 4C, or they could proceed directly to immunostaining.

Tissues were stained as described by Muntifering et al. (2018) with primary and secondary antibodies. To ensure even staining throughout the sample, antibodies were applied by using the SWITCH protocol (Murray et al., 2015). All incubations took place at 30C. Briefly, tissues were incubated for 6 days in IHC buffer with 0.5 mM SDS containing CK19 antibody (1:10 dilution). Tissues were then removed from the primary antibody solution and incubated for 1 day in IHC buffer without SDS. Tissues were washed in PBS 3 times for 2 hours each, then incubated in IHC buffer with 0.5mM SDS containing the corresponding conjugated secondary antibody for 6 days. Tissues were then removed from the secondary antibody solution and incubated for 1 day in IHC buffer without SDS. Tissues were washed in PBSA 3 times for 2 hours each, fixed for 2 hours in 4% PFA, washed once more in PBSA, and finally placed in CUBIC R2 solution (50wt% sucrose, 25wt% urea, 10wt% 2,2′,2′′-nitrilotriethanol, and 0.1% (v/v) Triton X-100) (Susaki et al., 2014) for imaging and long-term storage at room temperature.

All tissues were mounted in CUBIC R2 solution and imaged using an RSG4 ribbon scanning confocal microscope (Caliber, Andover, MA) as previously described by Watson et al. (2017). The microscope was fitted with a Nikon CFI90 20x glycerol-immersion objective (Nikon, Melville, NY) with 8.3mm working distance. Volumes were captured with voxel resolution of 0.467 × 0.467 × 12.2 μm (x, y, z). Laser intensity and detector settings were specific to each sample based on the levels of staining. In all cases, the intensity of the laser was increased in a linear manner throughout deeper focal planes to compensate for absorption of excitation and emission light. RAW images acquired in this way were stitched

and assembled into composites using a 24 node, 608 core cluster, then converted into the Imaris file format (Bitplane, Zurich, Switzerland). Volumes were rendered using Imaris v9.5.1.

RNA extraction and RNA-sequencing analysis—Frozen liver tissue was homogenized in Trizol at 4C and RNA was extracted using QIAGEN RNeasy Mini Kit (Cat. 74104). DNA digestion and removal were performed on the column using the RNase-free DNase Set (Cat. 79254) as per manufacturer instructions. RNA quality and concentration were assessed using a Nanodrop. Purified, high quality RNA from 6 WT livers (3 male, 3 female), and 6 YAP1 KO livers (3 male, 3 female) to Novogene Co. (Sacramento, CA) for cDNA library preparation and RNA-sequencing by Illumina Novaseq 6000 of paired-end 150bp reads, with 20 million reads per end per sample. Raw sequencing data was processed using CLC Genomics Workbench 20.0.3 (QIAGEN Inc., https://digitalinsights.qiagen.com) for quality control and aligned to the *Mus musculus* genome version GRCm38.p6. Reads assigned to each gene underwent TMM normalization and differential expression analysis was performed using *edgeR* within CLC Genomics to compare WT versus YAP1 KO mice. The top differentially expressed genes were filtered by adjusted p value $q < 0.05$ and fold-change greater than 2 for subsequent downstream pathway analysis using Ingenuity Pathway Analysis (IPA; QIAGEN Inc., https://digitalinsights.qiagen.com/products-overview/discovery-insights-portfolio/analysis-and-visualization/qiagen-ipa/), Gene Set Enrichment Analysis (GSEA) and Molecular Signature Database (MSigDB) (Subramanian et al., 2005), and Enrichr (Chen et al., 2013; Kuleshov et al., 2016). CLC Genomics Workbench, and IPA were all used under commercial licenses acquired by the University of Pittsburgh Health Sciences Library System.

Affymetrix microarray data analysis—We analyzed data collected using GeneChip® Mouse Genome 430 2.0 Array Set 430 (Affymetrix, Santa Clara, CA) from $YAP1^{fl/fl}$ mice treated with adeno-associated virus serotype 8 carrying either GFP or Cre-recombinase to create WT or hepatocyte-specific YAP1 knockout mice, previously published (GEO: GSE148607) (Bhushan et al., 2021). The raw CEL files were imported into R (version 3.5.0) using the *affy* package (Gautier et al., 2004). Probes were mapped to genes using the custom brain array CDF (Sandberg and Larsson, 2007). The *gcrma* package was used to perform GCRMA (Guanine Cytosine Robust Multi-Array Analysis) normalization (Wu and Irizarry, 2020). Genes with low expression (lowest 30%) or low variance (lowest 30%) were filtered out. Gene annotation information was added using the *annotate* and *mouse4302.db* packages (Carlson, 2016; Gentleman, 2018). Next, the *limma* package was used to apply an empirical Bayes statistical model to calculate a moderated t-statistic and p value for each gene comparing its log-fold expression in HB samples relative to the WT samples (Ritchie et al., 2015). Using an adjusted p value cutoff of 0.05, no differentially expressed genes were identified.

Measurement of bile flow through cannulation of the common bile duct and india ink injection—Animal work described in this manuscript has been approved and conducted under the oversight of the University of Pittsburgh Institutional Animal Care and Use Committee. The common bile duct was cannulated and the bile flow rate was measured

in live three to four month-old, male and female, WT and YAP1 KO mice. The bile duct was cannulated with a microfil tubing according to previously described techniques (Plaa and Becker, 1965; Tønsberg et al., 2010). In brief, mice were anesthetized with Avertin 0.5 mg/g intraperitoneally (IP). The common bile duct was incised with a pair of fine iridectomy scissors about 6 mm below the hilum of the liver. A microfil tube (WPI, Sarasota, FL, MF28G-5) was passed through the incision and propelled toward the hilum for a distance of about 3 mm. Bile flow rate was recorded (μl/min/100 g body weight) and bile was collected in CryoTube vials (Thermo Fisher Scientific) and immediately placed in liquid nitrogen.

A similar protocol was used to cannulate the common bile duct and inject about 1mL of black india ink (Higgins) into the biliary system of WT and YAP1 KO mice. The common bile duct was then tied off with 3.0 suture and livers were harvested. Treated livers were placed in 4% paraformaldehyde for 24 hours, then washed in PBS. Livers were then placed in 50% methanol for 4 hours, 100% methanol for 4 hours, and then a 1:1 mixture of benzyl alcohol and benzyl benzoate (BABB) as described previously (Walter et al., 2012). Images were taken on a Nikon stereomicroscope.

Bile acid species detection and quantification—Bile acid profiling was performed as described previously (Zhu et al., 2018). For liver tissue samples, livers were homogenized in water (100 mg tissue in 500 μL water), and then 300 μL of methanol: acetonitrile (v/v, 1:1) was added to a 100 μL aliquot of liver homogenate. For serum samples, 25 μL serum was mixed with 100 μL of methanol: acetonitrile (v/v, 1:1). All the mixtures were vortexed for 2 min and centrifuged at 15,000 rpm for 10 minutes. Two microliter of the supernatants from all samples was injected into the ultra-performance liquid chromatography (UPLC) coupled with a SYNAPT G2-S quadrupole time-of-flight mass spectrometry (Waters Corporation, Milford, MA) for analysis. The column type is Acquity UPLC BEH C18 column (2.1 × 100 mm, 1.7 μm). The details of mobile phase gradient were reported previously (Jiang et al., 2015). The QTOFMS system was operated in a negative high-resolution mode with electrospray ionization as described previously (Zhu et al., 2018). Bile acid species were quantified by measuring their relative abundance as the area under the curve for each species using standards for comparison. WT and YAP1 KO liver samples or serum samples were compared using a t test followed by Benjamini-Hochberg correction for multiple hypothesis testing, using FDR < 0.1 as a cutoff for significance.

Quantitative liver intravital imaging—Surgical methods used for the intravital imaging were described previously by Pradhan-Sundd et al. (2018). Intravascular fluorescent dyes included 100 μg of Carboxyflurescein (CF) and 200 μg of TXR dextran. TXR dextran (MW 70,000) was used to visualize the blood flow through the liver sinusoids whereas CF (MW 377) was used to visualize uptake of the dye from blood to hepatocytes at 1–2 m post-injection and then from the hepatocyte to the bile-canaliculi within 5 m. Microscopy was performed using a Nikon MPE multi-photon excitation microscope. Movies were processed using Nikon's NIS Elements (Nikon Elements 3.10). Signal contrast in each channel of a multicolor image was further enhanced by adjusting the maxima and minima of the intensity histogram of that channel. A median filter with a kernel size of 3 was applied over each video frame to improve signal-to-noise ratio.

QUANTIFICATION AND STATISTICAL ANALYSIS

Statistical details of each experiment can be found in the respective figure legends. Data are presented as mean ± standard deviation (sd). n refers to biological replicates. $p < 0.05$ was considered statistically significant, except for individual bile acid species comparisons for which an FDR of 0.1 was used. GraphPad PRISM 7.0c software was used for statistical analyses. No samples or animals were excluded from the analysis. Littermate controls of both genders were used throughout the study. Data significance was analyzed using a two-tailed unpaired Student's t test or Mann-Whitney test in cases where two groups were being compared. In cases where more than two groups were being compared, one-way or two-way ANOVA were used with Sidak's test to correct for multiple comparisons. For quantification of immunostaining, 3–5 20x fields from at least 3 mice of each group were analyzed, representing randomly selected regions from throughout all of the available tissue, and each dot graphed represents the average counts per mouse of all the fields combined.

Supplementary Material

Refer to Web version on PubMed Central for supplementary material.

ACKNOWLEDGMENTS

Funding was provided by grants 2T32EB001026-16A1 and 1F30DK121393-01A1 to L.M.M. and grants 5R01CA204586-05, 1R01DK62277, and the Endowed Chair for Experimental Pathology to S.P.M. and NIH grant 1P30DK120531-01 to the Pittsburgh Liver Research Center (for services provided by the Advanced Cell and Tissue Imaging Core). The study was also funded in part by grant 2P30CA047904-32 to S.W. and the Center for Biologic Imaging. We thank Dr. Frederic Lemaigre and Dr. Dean Yimlamai for numerous insightful discussions and feedback.

REFERENCES

Airik M, Schüler M, McCourt B, Weiss AC, Herdman N, Lüdtke TH, Widmeier E, Stolz DB, Nejak-Bowen KN, Yimlamai D, et al. (2020). Loss of Anks6 leads to YAP deficiency and liver abnormalities. Hum. Mol. Genet 29, 3064–3080. [PubMed: 32886109]

Alder O, Cullum R, Lee S, Kan AC, Wei W, Yi Y, Garside VC, Bilenky M, Griffith M, Morrissy AS, et al. (2014). Hippo signaling influences HNF4A and FOXA2 enhancer switching during hepatocyte differentiation. Cell Rep. 9, 261–271. [PubMed: 25263553]

Alvaro D, Mancino MG, Glaser S, Gaudio E, Marzioni M, Francis H, and Alpini G (2007). Proliferating cholangiocytes: a neuroendocrine compartment in the diseased liver. Gastroenterology 132, 415–431. [PubMed: 17241889]

Andersson ER, Chivukula IV, Hankeova S, Sjöqvist M, Tsoi YL, Ramsköld D, Masek J, Elmansuri A, Hoogendoorn A, Vazquez E, et al. (2018). Mouse Model of Alagille Syndrome and Mechanisms of Jagged1 Missense Mutations. Gastroenterology 154, 1080–1095. [PubMed: 29162437]

Antoniou A, Raynaud P, Cordi S, Zong Y, Tronche F, Stanger BZ, Jacquemin P, Pierreux CE, Clotman F, and Lemaigre FP (2009). Intrahepatic bile ducts develop according to a new mode of tubulogenesis regulated by the transcription factor SOX9. Gastroenterology 136, 2325–2333. [PubMed: 19403103]

Bhushan B, Molina L, Koral K, Stoops JW, Mars WM, Banerjee S, Orr A, Paranjpe S, Monga SP, Locker J, and Michalopoulos GK (2021). Yes-associated protein is crucial for constitutive androstane receptor-driven hepatocyte proliferation but not for induction of drug metabolism genes in mice. Hepatology 73, 2005–2022. [PubMed: 32794202]

Bray NL, Pimentel H, Melsted P, and Pachter L (2016). Near-optimal probabilistic RNA-seq quantification. Nat. Biotechnol 34, 525–527. [PubMed: 27043002]

Carlson M (2016). mouse4302.db: Affymetrix Mouse Genome 430 2.0 Array annotation data (chip mouse4302) (Bioconductor).

Chen EY, Tan CM, Kou Y, Duan Q, Wang Z, Meirelles GV, Clark NR, and Ma'ayan A (2013). Enrichr: interactive and collaborative HTML5 gene list enrichment analysis tool. BMC Bioinformatics 14, 128. [PubMed: 23586463]

Chung K, Wallace J, Kim SY, Kalyanasundaram S, Andalman AS, Davidson TJ, Mirzabekov JJ, Zalocusky KA, Mattis J, Denisin AK, et al. (2013). Structural and molecular interrogation of intact biological systems. Nature 497, 332–337. [PubMed: 23575631]

Clotman F, Jacquemin P, Plumb-Rudewiez N, Pierreux CE, Van der Smissen P, Dietz HC, Courtoy PJ, Rousseau GG, and Lemaigre FP (2005). Control of liver cell fate decision by a gradient of TGF beta signaling modulated by Onecut transcription factors. Genes Dev. 19, 1849–1854. [PubMed: 16103213]

Emerick KM, Rand EB, Goldmuntz E, Krantz ID, Spinner NB, and Piccoli DA (1999). Features of Alagille syndrome in 92 patients: frequency and relation to prognosis. Hepatology 29, 822–829. [PubMed: 10051485]

Fitamant J, Kottakis F, Benhamouche S, Tian HS, Chuvin N, Parachoniak CA, Nagle JM, Perera RM, Lapouge M, Deshpande V, et al. (2015). YAP inhibition restores hepatocyte differentiation in advanced HCC, leading to tumor regression. Cell Rep. 10, 1692–1707. [PubMed: 25772357]

Gautier L, Cope L, Bolstad BM, and Irizarry RA (2004). affy—analysis of Affymetrix GeneChip data at the probe level. Bioinformatics 20, 307–315. [PubMed: 14960456]

Gentleman R (2018). annotate: Annotation for microarrays (Bioconductor).

Gérard C, Tys J, and Lemaigre FP (2017). Gene regulatory networks in differentiation and direct reprogramming of hepatic cells. Semin. Cell Dev. Biol 66, 43–50. [PubMed: 27979774]

Heuman DM (1989). Quantitative estimation of the hydrophilic-hydrophobic balance of mixed bile salt solutions. J. Lipid Res 30, 719–730. [PubMed: 2760545]

Jiang C, Xie C, Li F, Zhang L, Nichols RG, Krausz KW, Cai J, Qi Y, Fang ZZ, Takahashi S, et al. (2015). Intestinal farnesoid X receptor signaling promotes nonalcoholic fatty liver disease. J. Clin. Invest 125, 386–402. [PubMed: 25500885]

Kamath BM, Munoz PS, Bab N, Baker A, Chen Z, Spinner NB, and Piccoli DA (2010). A longitudinal study to identify laboratory predictors of liver disease outcome in Alagille syndrome. J. Pediatr. Gastroenterol. Nutr 50, 526–530. [PubMed: 20421762]

Kamath BM, Ye W, Goodrich NP, Loomes KM, Romero R, Heubi JE, Leung DH, Spinner NB, Piccoli DA, Alonso EM, et al.; Childhood Liver Disease Research Network (ChiLDReN) (2020). Outcomes of Childhood Cholestasis in Alagille Syndrome: Results of a Multicenter Observational Study. Hepatol. Commun 4, 387–398. [PubMed: 33313463]

Katzenellenbogen M, Mizrahi L, Pappo O, Klopstock N, Olam D, Jacob-Hirsch J, Amariglio N, Rechavi G, Domany E, Galun E, and Goldenberg D (2007). Molecular mechanisms of liver carcinogenesis in the mdr2-knockout mice. Mol. Cancer Res 5, 1159–1170. [PubMed: 18025261]

Kim W, Khan SK, Gvozdenovic-Jeremic J, Kim Y, Dahlman J, Kim H, Park O, Ishitani T, Jho E-H, Gao B, and Yang Y (2017). Hippo signaling interactions with Wnt/b-catenin and Notch signaling repress liver tumorigenesis. J. Clin. Invest 127, 137–152. [PubMed: 27869648]

Kuleshov MV, Jones MR, Rouillard AD, Fernandez NF, Duan Q, Wang Z, Koplev S, Jenkins SL, Jagodnik KM, Lachmann A, et al. (2016). Enrichr: a comprehensive gene set enrichment analysis web server 2016 update. Nucleic Acids Res. 44 (W1), W90–W97. [PubMed: 27141961]

La Manno G, Soldatov R, Zeisel A, Braun E, Hochgerner H, Petukhov V, Lidschreiber K, Kastriti ME, Lönnerberg P, Furlan A, et al. (2018). RNA velocity of single cells. Nature 560, 494–498. [PubMed: 30089906]

Lee CS, Friedman JR, Fulmer JT, and Kaestner KH (2005). The initiation of liver development is dependent on Foxa transcription factors. Nature 435, 944–947. [PubMed: 15959514]

Lee D-H, Park JO, Kim T-S, Kim S-K, Kim T-H, Kim M-C, Park GS, Kim J-H, Kuninaka S, Olson EN, et al. (2016). LATS-YAP/TAZ controls lineage specification by regulating TGFβ signaling and Hnf4α expression during liver development. Nat. Commun 7, 11961. [PubMed: 27358050]

Lemaigre FP (2020). Development of the Intrahepatic and Extrahepatic Biliary Tract: A Framework for Understanding Congenital Diseases. Annu. Rev. Pathol 15, 1–22. [PubMed: 31299162]

Li H, Handsaker B, Wysoker A, Fennell T, Ruan J, Homer N, Marth G, Abecasis G, and Durbin R; 1000 Genome Project Data Processing Subgroup (2009). The Sequence Alignment/Map format and SAMtools. Bioinformatics 25, 2078–2079. [PubMed: 19505943]

Li X, Tao J, Cigliano A, Sini M, Calderaro J, Azoulay D, Wang C, Liu Y, Jiang L, Evert K, et al. (2015). Co-activation of PIK3CA and Yap promotes development of hepatocellular and cholangiocellular tumors in mouse and human liver. Oncotarget 6, 10102–10115. [PubMed: 25826091]

Lykavieris P, Hadchouel M, Chardot C, and Bernard O (2001). Outcome of liver disease in children with Alagille syndrome: a study of 163 patients. Gut 49, 431–435. [PubMed: 11511567]

Mansini AP, Peixoto E, Thelen KM, Gaspari C, Jin S, and Gradilone SA (2018). The cholangiocyte primary cilium in health and disease. Biochim. Biophys. Acta Mol. Basis Dis 1864 (4 Pt B), 1245–1253. [PubMed: 28625917]

Mao Q, Wang L, Tsang IW, and Sun Y (2017). Principal Graph and Structure Learning Based on Reversed Graph Embedding. IEEE Trans. Pattern Anal. Mach. Intell 39, 2227–2241. [PubMed: 28114001]

Michalopoulos GK, Barua L, and Bowen WC (2005). Transdifferentiation of rat hepatocytes into biliary cells after bile duct ligation and toxic biliary injury. Hepatology 41, 535–544. [PubMed: 15726663]

Mitchell E, Gilbert M, and Loomes KM (2018). Alagille Syndrome. Clin. Liver Dis 22, 625–641. [PubMed: 30266153]

Molina L, Yang H, Adebayo Michael AO, Oertel M, Bell A, Singh S, Chen X, Tao J, and Monga SPS (2019). mTOR inhibition affects Yap1-b-catenin-induced hepatoblastoma growth and development. Oncotarget 10, 1475–1490. [PubMed: 30863496]

Muntifering M, Castranova D, Gibson GA, Meyer E, Kofron M, and Watson AM (2018). Clearing for Deep Tissue Imaging. Curr. Protoc. Cytom 86, e38. [PubMed: 30005145]

Murray E, Cho JH, Goodwin D, Ku T, Swaney J, Kim SY, Choi H, Park YG, Park JY, Hubbert A, et al. (2015). Simple, Scalable Proteomic Imaging for High-Dimensional Profiling of Intact Systems. Cell 163, 1500–1514. [PubMed: 26638076]

Ober EA, and Lemaigre FP (2018). Development of the liver: Insights into organ and tissue morphogenesis. J. Hepatol 68, 1049–1062. [PubMed: 29339113]

Okabe H, Yang J, Sylakowski K, Yovchev M, Miyagawa Y, Nagarajan S, Chikina M, Thompson M, Oertel M, Baba H, et al. (2016). Wnt signaling regulates hepatobiliary repair following cholestatic liver injury in mice. Hepatology 64, 1652–1666. [PubMed: 27533619]

Pablo Arab J, Cabrera D, and Arrese M (2017). Bile Acids in Cholestasis and its Treatment. Ann. Hepatol 16 (Suppl 1), S53–S57.

Paranjpe S, Bowen WC, Mars WM, Orr A, Haynes MM, DeFrances MC, Liu S, Tseng GC, Tsagianni A, and Michalopoulos GK (2016). Combined systemic elimination of MET and epidermal growth factor receptor signaling completely abolishes liver regeneration and leads to liver decompensation. Hepatology 64, 1711–1724. [PubMed: 27397846]

Patel SH, Camargo FD, and Yimlamai D (2017). Hippo Signaling in the Liver Regulates Organ Size, Cell Fate, and Carcinogenesis. Gastroenterology 152, 533–545. [PubMed: 28003097]

Pepe-Mooney BJ, Dill MT, Alemany A, Ordovas-Montanes J, Matsushita Y, Rao A, Sen A, Miyazaki M, Anakk S, Dawson PA, et al. (2019). Single-Cell Analysis of the Liver Epithelium Reveals Dynamic Heterogeneity and an Essential Role for YAP in Homeostasis and Regeneration. Cell Stem Cell 25, 23–38.e8. [PubMed: 31080134]

Plaa GL, and Becker BA (1965). Demonstration of bile stasis in the mouse by a direct and an indirect method. J. Appl. Physiol 20, 534–537. [PubMed: 5837569]

Postic C, and Magnuson MA (2000). DNA excision in liver by an albumin-Cre transgene occurs progressively with age. Genesis 26, 149–150. [PubMed: 10686614]

Pradhan-Sundd T, Vats R, Russell JO, Singh S, Michael AA, Molina L, Kakar S, Cornuet P, Poddar M, Watkins SC, et al. (2018). Dysregulated Bile Transporters and Impaired Tight Junctions During Chronic Liver Injury in Mice. Gastroenterology 155, 1218–1232.e24. [PubMed: 29964040]

Ritchie ME, Phipson B, Wu D, Hu Y, Law CW, Shi W, and Smyth GK (2015). limma powers differential expression analyses for RNA-sequencing and microarray studies. Nucleic Acids Res. 43, e47. [PubMed: 25605792]

Sandberg R, and Larsson O (2007). Improved precision and accuracy for microarrays using updated probe set definitions. BMC Bioinformatics 8, 48. [PubMed: 17288599]

Schaub JR, Huppert KA, Kurial SNT, Hsu BY, Cast AE, Donnelly B, Karns RA, Chen F, Rezvani M, Luu HY, et al. (2018). *De novo* formation of the biliary system by TGFβ-mediated hepatocyte transdifferentiation. Nature 557, 247–251. [PubMed: 29720662]

Schindelin J, Arganda-Carreras I, Frise E, Kaynig V, Longair M, Pietzsch T, Preibisch S, Rueden C, Saalfeld S, Schmid B, et al. (2012). Fiji: an open-source platform for biological-image analysis. Nat. Methods 9, 676–682. [PubMed: 22743772]

Sekiya S, and Suzuki A (2014). Hepatocytes, rather than cholangiocytes, can be the major source of primitive ductules in the chronically injured mouse liver. Am. J. Pathol 184, 1468–1478. [PubMed: 24594350]

Stuart T, Butler A, Hoffman P, Hafemeister C, Papalexi E, Mauck WM 3rd, Hao Y, Stoeckius M, Smibert P, and Satija R (2019). Comprehensive Integration of Single-Cell Data. Cell 177, 1888–1902. [PubMed: 31178118]

Su X, Shi Y, Zou X, Lu Z-N, Xie G, Yang JYH, Wu C-C, Cui X-F, He K-Y, Luo Q, et al. (2017). Single-cell RNA-Seq analysis reveals dynamic trajectories during mouse liver development. BMC Genomics 18, 946. [PubMed: 29202695]

Subramanian A, Tamayo P, Mootha VK, Mukherjee S, Ebert BL, Gillette MA, Paulovich A, Pomeroy SL, Golub TR, Lander ES, and Mesirov JP (2005). Gene set enrichment analysis: a knowledge-based approach for interpreting genome-wide expression profiles. Proc. Natl. Acad. Sci. USA 102, 15545–15550. [PubMed: 16199517]

Susaki EA, Tainaka K, Perrin D, Kishino F, Tawara T, Watanabe TM, Yokoyama C, Onoe H, Eguchi M, Yamaguchi S, et al. (2014). Whole-brain imaging with single-cell resolution using chemical cocktails and computational analysis. Cell 157, 726–739. [PubMed: 24746791]

Tan X, Yuan Y, Zeng G, Apte U, Thompson MD, Cieply B, Stolz DB, Michalopoulos GK, Kaestner KH, and Monga SPS (2008). Beta-catenin deletion in hepatoblasts disrupts hepatic morphogenesis and survival during mouse development. Hepatology 47, 1667–1679. [PubMed: 18393386]

Tanimizu N, Kikkawa Y, Mitaka T, and Miyajima A (2012). α1- and α5-containing laminins regulate the development of bile ducts via b1 integrin signals. J. Biol. Chem 287, 28586–28597. [PubMed: 22761447]

Tao J, Calvisi DF, Ranganathan S, Cigliano A, Zhou L, Singh S, Jiang L, Fan B, Terracciano L, Armeanu-Ebinger S, et al. (2014). Activation of b-catenin and Yap1 in human hepatoblastoma and induction of hepatocarcinogenesis in mice. Gastroenterology 147, 690–701. [PubMed: 24837480]

Thakurdas SM, Lopez MF, Kakuda S, Fernandez-Valdivia R, Zarrin-Khameh N, Haltiwanger RS, and Jafar-Nejad H (2016). Jagged1 heterozygosity in mice results in a congenital cholangiopathy which is reversed by concomitant deletion of one copy of Poglut1 (Rumi). Hepatology 63, 550–565. [PubMed: 26235536]

Tharehalli U, Svinarenko M, Kraus JM, Kühlwein SD, Szekely R, Kiesle U, Scheffold A, Barth TFE, Kleger A, Schirmbeck R, et al. (2018). YAP Activation Drives Liver Regeneration after Cholestatic Damage Induced by *Rbpj* Deletion. Int. J. Mol. Sci 19, 3801.

Tønsberg H, Holm R, Bjerregaard TG, Boll JB, Jacobsen J, and Müllertz A (2010). An updated and simplified method for bile duct cannulation of rats. Lab. Anim 44, 373–376. [PubMed: 20736319]

Trapnell C, Cacchiarelli D, Grimsby J, Pokharel P, Li S, Morse M, Lennon NJ, Livak KJ, Mikkelsen TS, and Rinn JL (2014). The dynamics and regulators of cell fate decisions are revealed by pseudotemporal ordering of single cells. Nat. Biotechnol 32, 381–386. [PubMed: 24658644]

Tschaharganeh DF, Chen X, Latzko P, Malz M, Gaida MM, Felix K, Ladu S, Singer S, Pinna F, Gretz N, et al. (2013). Yes-associated protein up-regulates Jagged-1 and activates the Notch pathway in human hepatocellular carcinoma. Gastroenterology 144, 1530–1542. [PubMed: 23419361]

Valencia-Mayoral P, Weber J, Cutz E, Edwards VD, and Phillips MJ (1984). Possible defect in the bile secretory apparatus in arteriohepatic dysplasia (Alagille's syndrome): a review with observations on the ultrastructure of liver. Hepatology 4, 691–698. [PubMed: 6745859]

Walter TJ, Sparks EE, and Huppert SS (2012). 3-dimensional resin casting and imaging of mouse portal vein or intrahepatic bile duct system. J. Vis. Exp 68, e4272.

Walter TJ, Vanderpool C, Cast AE, and Huppert SS (2014). Intrahepatic bile duct regeneration in mice does not require Hnf6 or Notch signaling through Rbpj. Am. J. Pathol 184, 1479–1488. [PubMed: 24631193]

Wang J, Dong M, Xu Z, Song X, Zhang S, Qiao Y, Che L, Gordan J, Hu K, Liu Y, et al. (2018). Notch2 controls hepatocyte-derived cholangiocarcinoma formation in mice. Oncogene 37, 3229–3242. [PubMed: 29545603]

Watson AM, Rose AH, Gibson GA, Gardner CL, Sun C, Reed DS, Lam LKM, St Croix CM, Strick PL, Klimstra WB, and Watkins SC (2017). Ribbon scanning confocal for high-speed high-resolution volume imaging of brain. PLoS ONE 12, e0180486. [PubMed: 28686653]

Wu J, and Irizarry R (2020). gcrma: Background Adjustment Using Sequence Information (Bioconductor).

Wu N, Nguyen Q, Wan Y, Zhou T, Venter J, Frampton GA, DeMorrow S, Pan D, Meng F, Glaser S, et al. (2017). The Hippo signaling functions through the Notch signaling to regulate intrahepatic bile duct development in mammals. Lab. Invest 97, 843–853. [PubMed: 28581486]

Yang L, Wang W-H, Qiu W-L, Guo Z, Bi E, and Xu C-R (2017). A single-cell transcriptomic analysis reveals precise pathways and regulatory mechanisms underlying hepatoblast differentiation. Hepatology 66, 1387–1401. [PubMed: 28681484]

Yanger K, Zong Y, Maggs LR, Shapira SN, Maddipati R, Aiello NM, Thung SN, Wells RG, Greenbaum LE, and Stanger BZ (2013). Robust cellular reprogramming occurs spontaneously during liver regeneration. Genes Dev. 27, 719–724. [PubMed: 23520387]

Yimlamai D, Christodoulou C, Galli GG, Yanger K, Pepe-Mooney B, Gurung B, Shrestha K, Cahan P, Stanger BZ, and Camargo FD (2014). Hippo pathway activity influences liver cell fate. Cell 157, 1324–1338. [PubMed: 24906150]

Zhang N, Bai H, David KK, Dong J, Zheng Y, Cai J, Giovannini M, Liu P, Anders RA, and Pan D (2010). The Merlin/NF2 tumor suppressor functions through the YAP oncoprotein to regulate tissue homeostasis in mammals. Dev. Cell 19, 27–38. [PubMed: 20643348]

Zhao Q, Yang R, Wang J, Hu DD, and Li F (2017). PPARa activation protects against cholestatic liver injury. Sci. Rep 7, 9967. [PubMed: 28855630]

Zhu J, Wang P, Shehu AI, Lu J, Bi H, and Ma X (2018). Identification of Novel Pathways in Idelalisib Metabolism and Bioactivation. Chem. Res. Toxicol 31, 548–555. [PubMed: 29896955]

Highlights

- YAP1 is expressed in hepatoblasts during liver development
- *Yap1* loss from hepatoblasts led to absent intrahepatic bile duct (IHBD) formation
- YAP1 is required for formation of the second layer of patent IHBD in development
- *Yap1* KO mice without IHBD survive by altering bile acid transport and metabolism

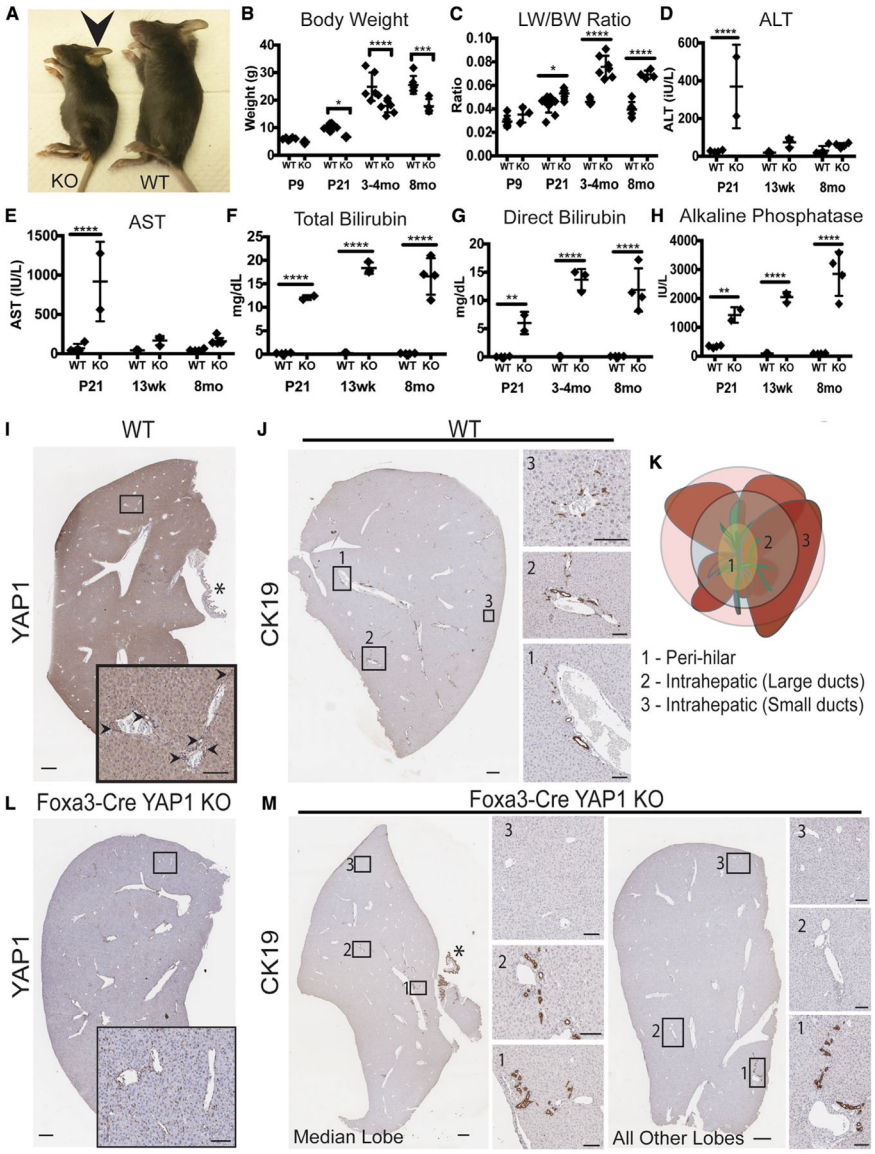

Figure 1. Loss of YAP1 in HBs leads to failure of intrahepatic bile duct formation

(A) Gross image of WT and YAP1 KO mouse. The arrow shows jaundiced ears.

(B and C) Body weight (B) and liver weight-to-body weight (LW/BW) ratio (C) of WT and KO mice over time.

(D–H) Serum levels of (D) alanine aminotransferase (ALT), (E) aspartate aminotransferase (AST), (F) total bilirubin, (G) direct bilirubin, and (H) alkaline phosphatase in WT and KO mice over time. Graphs show mean ± SD. Data were analyzed by 2-way ANOVA with Sidak multiple comparison test, n = 2–5 mice per group (*p <0.05, **p < 0.01, ***p < 0.001, ****p < 0.0001).

(I) IHC for YAP1 in WT mice. Arrows show nuclear YAP1 in bile ducts.

(J and K) CK19 marks bile ducts in the liver (J) spanning the three main regions described in (K).

(L) IHC for YAP1 in KO mice.

(M) CK19 staining in various lobes of YAP1 KO mice. Asterisks mark the gallbladders. (I)–(M) represent adult mice age 3–4 months old. Scale bars are 500 μm for whole lobes, 100 μm for insets.

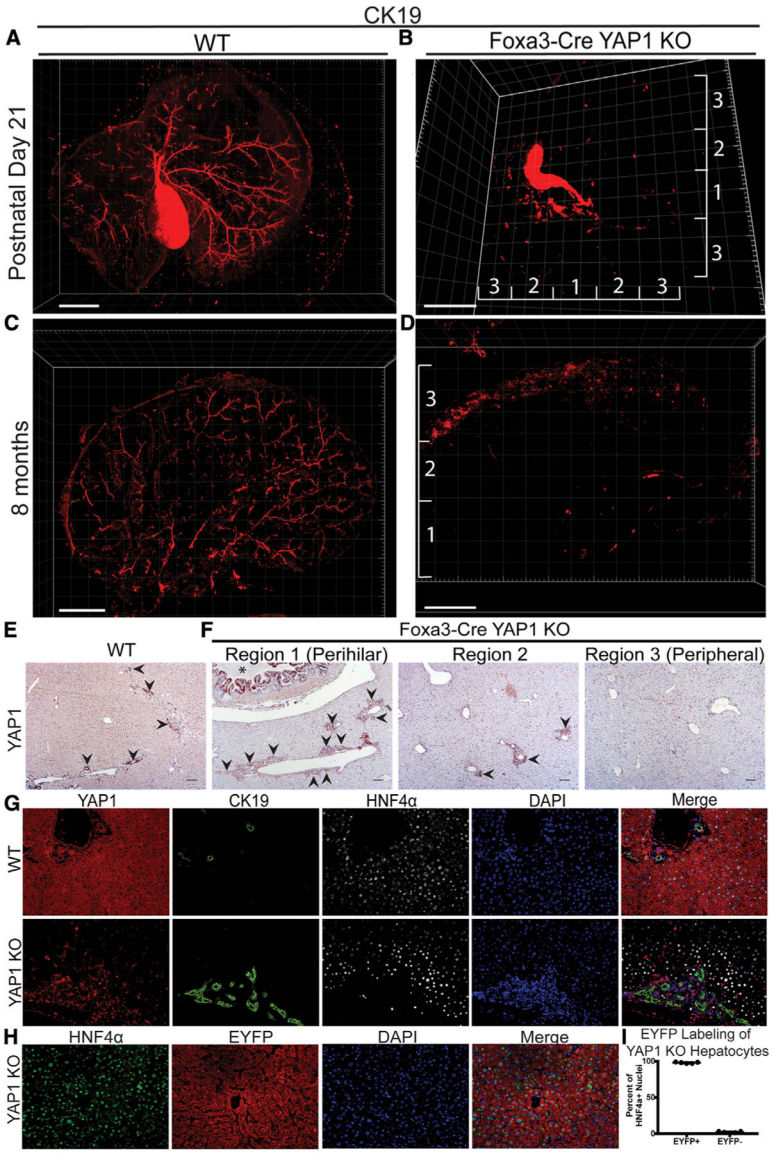

Figure 2. YAP1 KO mice show no long-term regeneration of bile ducts and no transdifferentiation of hepatocytes into cholangiocytes

(A–D) IF for CK19 followed by ribbon-confocal scanning microscopy illustrates in 3D the mature biliary tree of WT mice at (A) P21 and (C) 8 months of age and shows the absence of bile ducts in YAP1 KO mice at (B) P21 and (D) 8 months of age. Scale bars are 2 mm. Regions 1, 2, and 3 refer approximately to the expected positions of perihilar ducts, intrahepatic large ducts, and intrahepatic small ducts, respectively.

(E) IHC for YAP1 in adult WT mice. Arrows highlight bile ducts.

(F) IHC for YAP1 in adult KO mice. Arrows highlight ductular reaction. Scale bars are 100 μm.

(G) IF co-staining for YAP1, CK19, and HNF4α in WT and YAP1 KO mice (203 magnification).

(H) IF co-staining for HNF4α and EYFP in YAP1 KO mice (20× magnification).

(I) Quantification of EYFP-positive, HNF4α-positive cells in adult YAP1 KO mice (mean ± SD, n = 5 mice, representing the average of 3–5 20× fields per mouse).

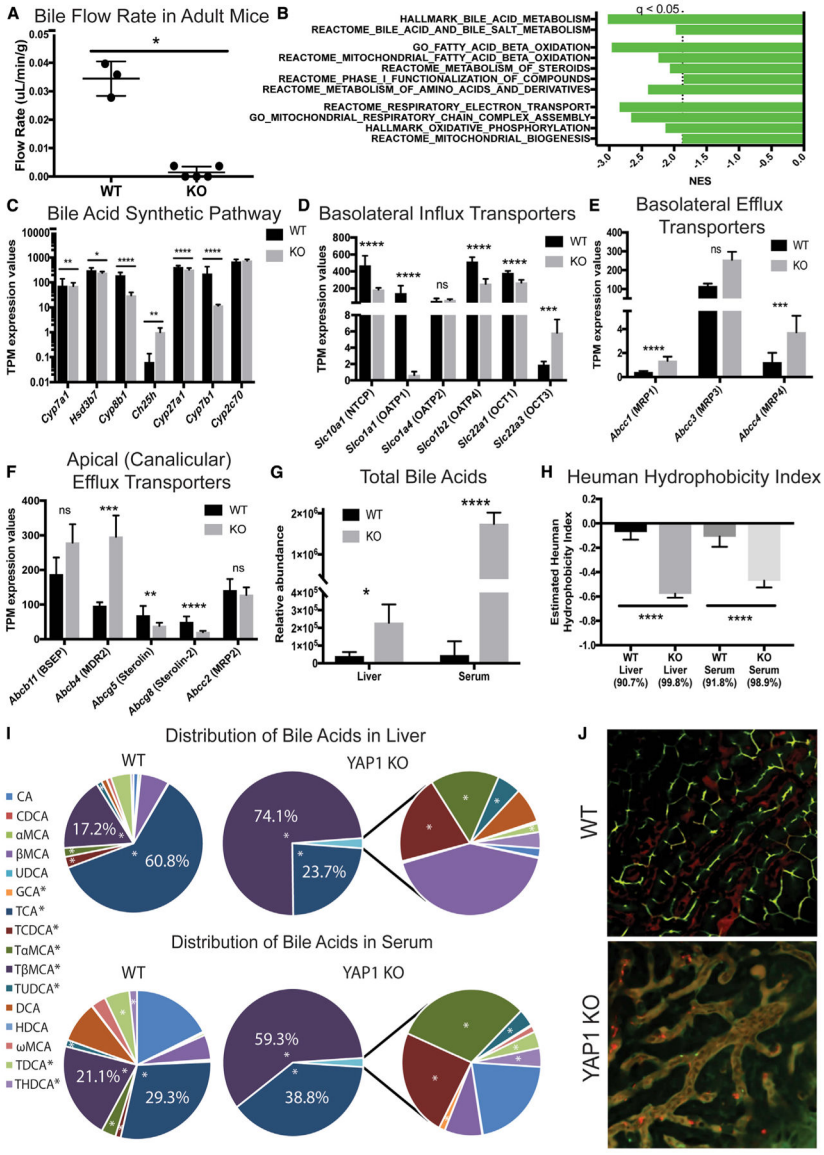

Figure 3. YAP1 KO mice adapt to chronic cholestasis by reducing bile acid toxicity and secreting them into the bloodstream

(A) Cannulation of the common bile duct was used to measure baseline bile flow in adult WT and YAP1 KO mice (3–5 mice per group, two-tailed Mann-Whitney test, *p < 0.05).

(B) GSEA revealed several metabolic pathways negatively enriched in YAP1 KO mice versus WT.

(C–F) RNA-seq analysis shows altered gene expression of genes related to bile acid synthesis and excretion (*q < 0.05, **q < 0.01, ***q < 0.001, ****q < 0.0001).

(G) Mass spectrometry was used to measure the abundance of bile acid species in liver tissue and serum from WT and YAP1 KO mice (n of 8 WT with 4 males and 4 females and 7 KO with 4 males and 3 females; data show mean ± SD; 2-way ANOVA with Sidak multiple comparison test, *p < 0.05, ****p < 0.0001).

(H) Hydrophobicity index of the bile acid pool in liver and serum was calculated based on the Heuman index values for each bile acid species (Heuman, 1989) (mean ± SD, t test,

****$p < 0.0001$). Underneath, we include the percentages of total bile acids used in each calculation, because the index values for certain species are unavailable.

(I) Average distribution and abundance of murine bile acid species are shown for WT and YAP1 mice. Asterisks refer to conjugated bile acids.

(J) Still shots taken from live movies (Video S2) from intravital microscopy, showing the circulation of blood and bile in both WT and YAP1 KO mice.

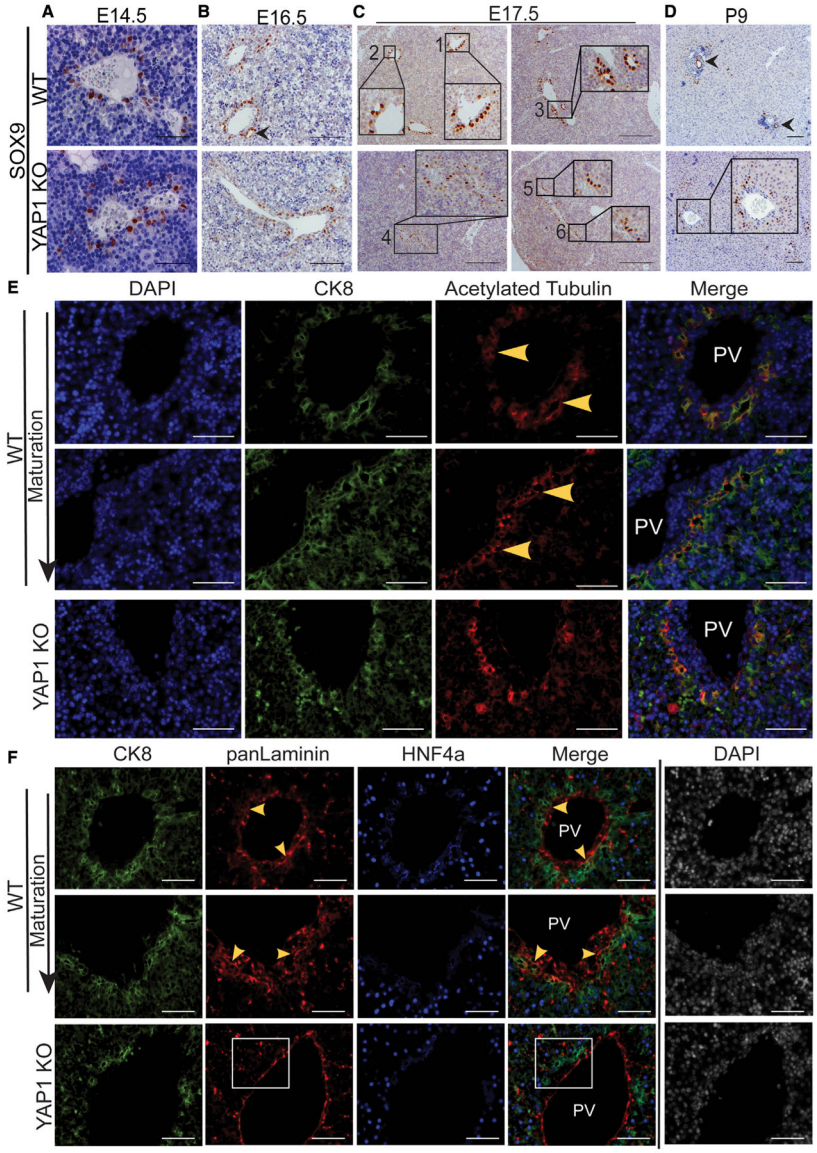

Figure 4. YAP1 KO leads to defective bile duct morphogenesis in late liver development

(A–D) IHC for SOX9 in WT and YAP1 KO livers at (A) E14.5, (B) E16.5, (C) E17.5, and (D) P9. Arrows and insets point to various stages of bile duct development as described in the text.

(E) IF co-staining for CK8 and acetylated tubulin at E17.5 in WT and YAP1 KO livers, showing bile ducts at intermediate stages of maturation. Yellow arrows highlight punctate tubulin staining marking primary cilia.

(F) IF co-staining for CK8, pan-laminin, and HNF4α at E17.5 in WT and YAP1 KO livers, showing bile ducts at intermediate stages of maturation. Yellow arrows mark laminin deposition in the basement membrane of maturing WT ducts, whereas white boxes show an immature duct in KO mice with no laminin deposition. Scale bars are (A, E, and F) 50 μm and (B–D) 100 μm. Representative images chosen after analyzing n = 3–4 mice in each group.

Table 1.

Observed and expected genotype frequencies from breeding YAP1 KO mice

		WT	HET	YAP1 KO	Total
Embryos	observed	47	19	27	93
	expected	46.5	23.25	23.25	93
Chi-square test	p value	0.4998			
Adult	observed	172	75	47	294
	expected	147	73.5	73.5	294
Chi-square test	p value	0.0009894			

KEY RESOURCES TABLE

REAGENT or RESOURCE	SOURCE	IDENTIFIER
Antibodies		
Rabbit monoclonal anti-YAP1	Cell Signaling Technology	Cat#CS14074; RRID: AB_2650491
Rat monoclonal anti-CK19 (Cytokeratin 19)	Developmental Studies Hybridoma Bank (DSHB)	Cat#TROMAIII; RRID: AB_2133570
Rabbit polyclonal anti-SOX9	EMD Millipore	Cat#ab5535; RRID: AB_2239761
Rat monoclonal anti-CD45	Santa Cruz Biotechnology	Cat#sc-53665; RRID: AB_629093
Mouse monoclonal anti-HNF4α	R&D Systems	Cat#PP-H1415-00; RRID: AB_2263954
Rabbit monoclonal anti-HNF4α	Cell Signaling Technology	Cat#CS3113; RRID: AB_2295208
Chicken polyclonal anti-GFP/EYFP	Abcam	Cat#ab13970; RRID: AB_300798
Rat monoclonal anti-CK8 (Cytokeratin 8)	DSHB	Cat#TROMAI; RRID: AB_531826
Mouse monoclonal anti-Acetylated α-tubulin	Sigma Aldrich	Cat#T6793; RRID: AB_477585
Rabbit polyclonal anti-pan-laminin	Sigma Aldrich	Cat#L9393; RRID: AB_477163
Mouse monoclonal anti-JAGGED1	Santa Cruz Biotechnology	Cat# sc-390177; RRID: AB_2892141
Mouse monoclonal anti-CEACAM1	LSBio	Cat# LS-C106710; RRID: AB_10625970
Rat monoclonal anti-EpCAM	BioLegend	Cat#118201; RRID: AB_1089026
Mouse monoclonal anti-HES1	Santa Cruz Biotechnology	Cat#sc-166410; RRID: AB_2117960
Donkey anti-Rat IgG (H+L) Highly Cross-Adsorbed Secondary Antibody, Alexa Fluor 488	Invitrogen	Cat#A-21208; RRID: AB_2535794
Donkey anti-Rabbit IgG (H+L) Highly Cross-Adsorbed Secondary Antibody, Alexa Fluor Plus 555	Invitrogen	Cat#A-32794; RRID: AB_2762834
Goat anti-Mouse IgG (H+L) Cross-Adsorbed Secondary Antibody, Alexa Fluor 647	Invitrogen	Cat#A-21235; RRID: AB_2535804
Goat anti-Chicken IgY (H+L) Cross-Adsorbed Secondary Antibody, Alexa Fluor Plus 555	Invitrogen	Cat#A-32932; RRID: AB_2762844
Goat anti-Rabbit IgG (H+L) Highly Cross-Adsorbed Secondary Antibody, Alexa Fluor Plus 647	Invitrogen	Cat#A-32733; RRID: AB_2633282
Donkey anti-Mouse IgG (H+L) Highly Cross-Adsorbed Secondary Antibody, Alexa Fluor Plus 555	Invitrogen	Cat#A-32773; RRID: AB_2762848
IgG Donkey anti-Rabbit, Biotin, Polyclonal, Secondary Antibody	MilliporeSigma	Cat#AP182B; RRID: AB_92587
IgG Goat anti-Mouse, Biotin, Polyclonal, Secondary Antibody	MilliporeSigma	Cat#AP181B; RRID: AB_92577
IgG Goat anti-Rat, Biotin, Polyclonal, Secondary Antibody	MilliporeSigma	Cat#AP183B; RRID: AB_92595
Critical commercial assays		
RNeasy Mini Kit	QIAGEN	Cat#74104
Deposited data		
Raw and analyzed RNA-sequencing data	This paper	GEO: GSE157777
Raw Affymetrix microarray data	Bhushan et al., 2021	GEO: GSE148607
Experimental models: Organisms/strains		
Mouse: Foxa3-Cre YAP1 KO [Tg(Foxa3-Cre)1Khk, Yap1$^{tm1.1Dupa}$, Gt(ROSA)26Sor$^{tm1(EYFP)Cos}$/J]	This paper	N/A
Mouse: B6.129X1-Gt(ROSA)26Sor$^{tm1(EYFP)Cos}$/J	The Jackson Laboratory	JAX: 006148
Mouse: B6.129P2(Cg)-Yap1$^{tm1.1\ Dupa}$/J	The Jackson Laboratory	JAX: 032192

REAGENT or RESOURCE	SOURCE	IDENTIFIER
Mouse: Tg(Foxa3-cre)1Khk	Tan et al., 2008	MGI:2664968
Software and algorithms		
CLC Genomics Workbench 20.0.3	QIAGEN	https://digitalinsights.qiagen.com
Ingenuity Pathway Analysis	QIAGEN	https://digitalinsights.qiagen.com/products-overview/discovery-insights-portfolio/analysis-and-visualization/qiagen-ipa/
Gene Set Enrichment Analysis	UC San Diego/Broad Institute	https://www.gsea-msigdb.org/gsea/index.jsp
Enrichr	Ma'ayan Lab	https://maayanlab.cloud/Enrichr/
Nikon NIS Elements 3.10	Nikon	https://www.microscope.healthcare.nikon.com/products/software/nis-elements/
IMARIS v9.5.1	Oxford Instruments	https://imaris.oxinst.com
Fiji/ImageJ	Schindelin et al., 2012	https://imagej.net/software/fiji/
SRA-Tools	NCBI	http://ncbi.github.io/sra-tools/
kallisto	Bray et al., 2016	N/A
SAMtools	Li et al., 2009	N/A
Velocyto	La Manno et al., 2018	N/A
Seurat	Stuart et al., 2019	N/A
Monocle	Trapnell et al., 2014	N/A
Adobe Creative Cloud (Illustrator, Photoshop)	Adobe	https://www.adobe.com/creativecloud.html
ObjectiveView	Objective Pathology Services	https://www.objectivepathology.com/objectiveview
GraphPad PRISM 7.0c	GraphPad	https://www.graphpad.com
affy	Gautier et al., 2004	N/A
gcrma	Wu and Irizarry, 2020	N/A
annotate	Gentleman, 2018	N/A
mouse4302.db	Carlson, 2016	N/A
limma	Ritchie et al., 2015	N/A